The Astrophysical Journal, 1006:100 (9pp), 2026 July 20 https://doi.org/10.3847/1538-4357/ae8028

Alpha-particle Heating and Anisotropy in Solar Wind Turbulence: Insights from Parker Solar Probe Observations and Particle-in-cell Simulations

Q. Y. Xiong[1], S. Y. Huang[1], Z. G. Yuan[1], G. Li[2], J. S. He[3], N. Bian[2], D. Verscharen[4], T. N. Parashar[5], J. Zhang[6], H. H. Wu[1], K. Jiang[1], and H. W. Zhan[1]
[1] School of Earth and Space Science and Technology, Wuhan University, Wuhan, 430072, People's Republic of China; shiyonghuang@whu.edu.cn
[2] State Key Laboratory of Lunar and Planetary Sciences, Macau University of Science and Technology, Macau, People's Republic of China
[3] Institute of Space Physics and Applied Technology, Peking University, Beijing, People's Republic of China
[4] Mullard Space Science Laboratory, University College London, Surrey, UK
[5] Victoria University of Wellington, Kelburn, Wellington, 6012, New Zealand
[6] State Key Laboratory of Marine Geology, School of Ocean and Earth Science, Tongji University, Shanghai, 200092, People's Republic of China
Received 2026 May 2; revised 2026 June 8; accepted 2026 June 19; published 2026 July 17

Abstract

Alongside protons, alpha particles make up a crucial part of the solar wind's ion population, playing an important role in turbulent energy conversion and ion-scale heating. However, the physical processes governing their temperature evolution, anisotropy development, and differential streaming remain incompletely understood. Using Parker Solar Probe observations and 2.5D particle-in-cell simulations, we investigate how the alpha–proton temperature ratio regulates the subsequent alpha-particle heating efficiency and associated kinetic signatures. The observations reveal that alpha-particle heating and anisotropy are strongly modulated by the local value of the alpha–proton temperature ratio. The simulations reproduce these trends, showing that an increasing alpha–proton temperature ratio lowers the growth of alpha-particle thermal energy, anisotropy, and differential drift. These results demonstrate that the alpha-particle heating pathway could be self-regulated by its initial thermodynamic state, with hotter alpha particles remaining farther from the instability threshold and experiencing less resonant energization. Our findings provide new constraints on ion-scale dissipation in the near-Sun solar wind and offer a unified interpretation of alpha-proton heating.

Unified Astronomy Thesaurus concepts: Plasma astrophysics (1261); Plasma physics (2089); Space plasmas (1544); Interplanetary turbulence (830); Solar wind (1534)

1. Introduction

Turbulence is a fundamental and ubiquitous phenomenon in fluids and plasmas, characterized by the nonlinear interactions among fluctuations spanning a wide range of spatial and temporal scales (U. Frisch 1995; D. Biskamp 2003; G. Li et al. 2011; K. H. Kiyani et al. 2015; S. Y. Huang et al. 2022). In plasma, turbulence mediates the transfer of energy from large-scale motions to smaller scales. At larger scales, it is injected by processes such as solar activity or flow instability; at smaller scales, it is ultimately dissipated and converted into particle heating and acceleration (C.-Y. Tu & E. Marsch 1995; F. Sahraoui et al. 2009; A. A. Schekochihin et al. 2009; R. Bruno & V. Carbone 2013; S. Y. Huang et al. 2023). These processes play a crucial role in regulating the transport of mass, momentum, and energy in various astrophysical environments, including planetary magnetospheres (L. Z. Hadid et al. 2015; S. Y. Huang et al. 2017; T. A. Bowen et al. 2021), accretion disks (S. A. Balbus & J. F. Hawley 1998), and the solar wind (W. H. Matthaeus & M. Velli 2011; D. Verscharen et al. 2019). In the solar wind, turbulence exhibits a broad inertial range consistent with the magnetohydrodynamic (MHD) scaling at large scales, which transitions to a kinetic regime at proton and subion scales (F. Sahraoui et al. 2009, 2013; J. He et al. 2012; S. Y. Huang et al. 2021), where wave–particle interactions and kinetic instabilities become important (O. Alexandrova et al. 2009; C. H. K. Chen et al. 2019). These multiscale fluctuations are highly anisotropic with respect to the local magnetic field and exhibit complex couplings between velocity, magnetic, and density perturbations (T. S. Horbury et al. 2008; J. Zhang et al. 2022). These features make solar wind turbulence a natural laboratory for studying plasma heating and energy dissipation under collisionless conditions.

Foundational theoretical and observational frameworks have long established that energy cascades from large-scale MHD fluctuations, often driven by wave activity, down to dissipation scales where it is converted into thermal energy (W. H. Matthaeus et al. 1999; B. D. G. Chandran & J. C. Perez 2019). At these kinetic scales, resonant or nonresonant processes preferentially energize ions and drive temperature anisotropies (R. E. Navarro et al. 2020). However, as the solar wind expands, kinetic instabilities continuously act to constrain the ion temperature anisotropy and relative drift, thus regulating the macroscopic parameter evolution of the plasma (S. P. Gary et al. 2003). The Parker Solar Probe (PSP; N. J. Fox et al. 2016) and Solar Orbiter (SolO; D. Müller et al. 2020) missions have initiated a new era in heliospheric physics, allowing these long-standing theoretical frameworks to be tested directly in the near-Sun environment. Recent studies have provided unprecedented observational constraints on these kinetic processes, revealing the preferential energization of solar wind ions even below the Alfvénic surface (P. Mostafavi et al. 2025) and demonstrating the complex, nonmonotonic radial evolution of pressure tensor components in the young solar wind (L. Ofman Yogesh et al. 2026). Concurrently, comprehensive analyses of these novel datasets continue to probe the evolution of temperature anisotropies and their relation to local instabilities throughout the inner heliosphere (V. K. Jagarlamudi et al. 2025).

Alpha particles, or fully ionized helium nuclei, constitute the second-most abundant ion species in the solar wind, typically comprising about 3%–5% of the total ion number density (M. Neugebauer 1981; J. C. Kasper et al. 2007). Despite their relatively low proportion, alpha particles play a significant function in the dynamics of solar wind turbulence due to their higher mass and charge compared to protons, which enable them to carry a substantial ratio of the plasma momentum and energy flux (E. Marsch et al. 1982; L. Matteini et al. 2012). The alpha–proton temperature ratio (T_α/T_p) is generally greater than unity near the Sun and tends to decrease with heliocentric distance, suggesting preferential heating of alpha particles in the inner heliosphere (D. J. McComas et al. 2000; S. P. Gary et al. 2006; J. C. Kasper et al. 2008; D. Stansby et al. 2019). Both species exhibit temperature anisotropies with respect to the local magnetic field, often characterized by $T_\perp/T_\parallel > 1$ ($T_\perp$ and $T_\parallel$ denote perpendicular and parallel temperature), indicating perpendicular heating process likely associated with ion-cyclotron or mirror-mode instabilities (P. Hellinger et al. 2006; S. D. Bale et al. 2009; B. A. Maruca et al. 2012; L. Ofman et al. 2017). Another key feature is the differential flow between alpha particles and protons ($V_{\alpha p}$), which can reach up to local proton Alfvén speed and influence the development of instabilities such as Alfvénic ion-beam or fast-magnetosonic instabilities (S. Bourouaine et al. 2011a; D. Perrone et al. 2013). The participation of alpha particles in solar wind turbulence thus not only modifies the cascade and dissipation of turbulent energy but also affects the efficiency of ion heating and acceleration (A. Greco et al. 2015; L. Matteini et al. 2015).

Previous observations over a wide range of heliocentric distances have revealed that the thermal properties and anisotropies of alpha particles and protons in the solar wind exhibit systematic variations as the plasma expands from the Sun. These results are caused by the combined effects of adiabatic expansion, Coulomb relaxation, and kinetic instabilities (P. Hellinger et al. 2011). The recent PSP and SolO missions have extended these observations much closer to the Sun, reaching within 0.1 astronomical units (au) and uncovering the plasma conditions in the near-coronal environment (T. A. Bowen et al. 2020; J. S. Halekas et al. 2020; J. C. Kasper et al. 2021). These measurements show that both protons and alpha particles exhibit strong temperature anisotropies and elevated alpha–proton temperature ratios, consistent with preferential and ongoing heating in the inner heliosphere (J. Huang et al. 2020; L. D. Woodham et al. 2021). The instabilities associated with alpha particles and protons near perihelia are highly connected to the energy cascade to kinetic scales (L. Ofman et al. 2022). However, within sudden magnetic field reversals known as switchbacks, a correlation has also been found between the alpha-particle temperature and the magnetic field deflection. No such relation is observed for protons, indicating preferential heating of alpha particles (D. Perrone et al. 2024). These results from early and recent spacecraft highlight that the thermal evolution of solar wind ions is not merely governed by adiabatic expansion but is continuously influenced by turbulent dissipation and wave–particle interactions in the heliosphere.

Turbulence and the presence of multiple ion species, particularly alpha particles, play a fundamental role in shaping the thermodynamic evolution and kinetic properties of the solar wind (E. Marsch et al. 1982; J. C. Kasper et al. 2008). The interaction between turbulent fluctuations, wave–particle processes, and differential ion dynamics governs how energy is distributed among plasma species during their expansion through the heliosphere. With the advent of recent missions, it has become possible to probe the solar wind much closer to its source, revealing enhanced particle heating, strong temperature anisotropies, and complex kinetic signatures that were inaccessible to earlier observations. In this study, we utilize the complete set of PSP observations up to the latest available orbits to perform a statistical analysis of the alpha–proton temperature ratios and anisotropies as a function of heliocentric distance. Our results demonstrate clear radial trends that provide new insights into how differential heating and anisotropy evolve in the inner heliosphere. To further interpret these observational findings, we employ fully kinetic particle-in-cell (PIC) simulations to explore the underlying processes responsible for ion heating and anisotropy generation in turbulent plasmas. Our study strengthens the understanding of how turbulent processes and multi-ion interactions regulate energy partition and thermal anisotropy in the solar wind.

2. Observations

We primarily employ measurements from two instrument suites on PSP: the Solar Probe Analyzer-Ions (SPAN-I; J. C. Kasper et al. 2016; R. Livi et al. 2022) investigation and the FIELDS (S. D. Bale et al. 2016) instrument. SPAN-I records three-dimensional ion velocity distribution functions (VDFs) with a common time resolution of 3.5 s, using an electrostatic analyzer and time-of-flight (TOF) mass discrimination. It can distinguish between protons and alpha particles. Consequently, the plasma number density, bulk velocity, and temperature of each ion species can be derived from their respective VDFs. Meanwhile, FIELDS measures the magnetic fields with high cadence, where we adopt the data from fluxgate magnetometers (MAG), which can reach a maximum sampling rate of 293 Hz. We employ the data until 2024 September, encompassing encounter 21. During this period, PSP reached heliocentric distances around 0.05 au, providing extensive radial coverage for investigating the evolution of particles from near-Sun to heliospheric distances.

To ensure consistency among different datasets, we standardize the time base of all measurements using the sampling cadence of the SPAN-I alpha-particle data as the reference. The corresponding proton moments and magnetic field data from FIELDS are temporally aligned to this reference by applying linear interpolation or nearest-neighbor matching, while data points outside the overlapping intervals are discarded. This process ensures that each data record contains a synchronized set of alpha-particle, proton, and magnetic field measurements. In addition, only data points with nominal quality flags across all datasets are retained; records containing significant instrumental errors, such as counter overflows, active diagnostic tests, overdeflection, or invalid energy tables, in either the ion or magnetic field measurements, are strictly excluded from further analysis.

To ensure the reliability of the alpha-particle moments, we further applied a SPAN-I field-of-view (FOV) selection criterion following the approach used in recent PSP studies of alpha-particle properties (P. Mostafavi et al. 2022, 2024, 2025; L. Ofman Yogesh et al. 2026). SPAN-I is mounted on

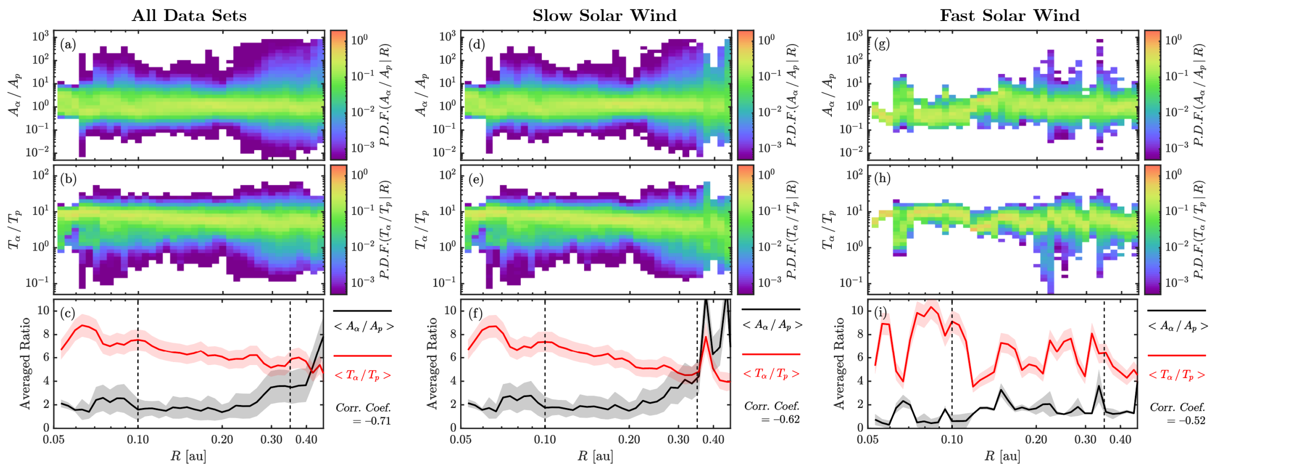

Figure 1. Radial evolution of the anisotropy ratio A_α/A_p and temperature ratio T_α/T_p from PSP observations. The three columns are the results from (a)–(c) all datasets, (d)–(f) slow solar wind, and (g)–(i) fast solar wind. The first two rows, (a)–(h), are the pdfs of A_α/A_p and T_α/T_p, respectively. The black and red curves in (c), (f), and (i) are the averaged values of A_α/A_p and T_α/T_p at each corresponding radial distance, respectively. The shaded regions accompanied by these two curves represent the error bar of standard deviation.

the ram-facing side of the PSP spacecraft, and the solar wind ion distributions are best measured when the spacecraft motion brings the core of the distribution into the instrument FOV (R. Livi et al. 2022). Therefore, reliable plasma moments require that the core of the ion velocity distribution, especially that of alpha particles, is well captured by SPAN-I rather than located near the edge of the angular coverage. Following this consideration, we retained only measurements for which the azimuthal peak of the ion distribution is located within the reliable SPAN-I FOV. Specifically, we required the peak azimuthal angle to satisfy $\phi = 163\overset{\circ}{.}125$, corresponding to the center of the last reliable azimuthal bin before the high-ϕ boundary at $168\overset{\circ}{.}75$. This additional FOV filter reduces possible edge-of-FOV effects in the derived alpha-particle temperature anisotropies.

The particle temperatures are computed from the temperature tensor components. The scalar temperature is calculated as $T_s = Tr(\boldsymbol{T}_s)/3$, where s represents the ion species, $\boldsymbol{T}_s$ is the temperature tensor, and Tr is the matrix trace. To determine the parallel and perpendicular temperatures with respect to the local magnetic field direction, the temperature tensor is rotated into a field-aligned coordinate system. Denoting the unit vector along the instantaneous magnetic field as $\hat{\boldsymbol{b}} = \boldsymbol{B}/|\boldsymbol{B}|$, the parallel and perpendicular temperatures are obtained by $T_{s,\parallel} = \hat{\boldsymbol{b}}^T \boldsymbol{T}_s \hat{\boldsymbol{b}}$ and $T_{s,\perp} = (Tr(\boldsymbol{T}_s) - T_{s,\parallel})/2$. Therefore, the particle temperature anisotropy is defined as $A_s = T_{s,\perp}/T_{s,\parallel}$. The alpha–proton differential velocity is calculated as the magnitude of the difference between the bulk velocities of the two species: $V_{\alpha p} = |\boldsymbol{U}_\alpha - \boldsymbol{U}_p|$.

In this study, we analyze the relative ratios of alpha-to-proton temperature T_a/T_p and anisotropy A_a/A_p rather than their isolated, absolute evolution. Because protons and alpha particles are colocated within the solar wind and exposed to identical background turbulence, they are likely to undergo fundamentally similar heating mechanisms. However, their distinct mass and charge dictate their coupling efficiencies at different kinetic scales, driving preferential heating (D. Verscharen et al. 2019; M. F. Zhang et al. 2025). Furthermore, by calculating these local ratios at each data point prior to our statistical binning, we normalize the measurements against macroscopic background variations, such as adiabatic expansion. This localized normalization ensures that our statistical results accurately isolate the preferential heating and anisotropy evolution driven by local turbulence, preventing the mix of kinetic effects with large-scale spatial variations in the solar wind.

Figure 1 presents the radial variations of the temperature ratio and anisotropy ratio between alpha particles and protons in the solar wind, which are derived from the dataset described above. First, Figures 1(a) and (b) show the conditional probability distribution functions (pdfs) of A_a/A_p and T_a/T_p as functions of the heliocentric distance R. These pdfs are constructed by binning all data points according to R, and then computing the normalized occurrence probability of each parameter within each radial bin. As shown in those two subpanels, A_a/A_p exhibits a rough increasing trend, indicating that the relative anisotropy of alpha particles becomes more pronounced as the solar wind expands outward. In contrast, T_a/T_p displays a decreasing trend, suggesting that the preferential heating of alpha particles relative to protons weakens farther from the Sun.

Furthermore, Figure 1(c) presents the mean radial profiles of the A_a/A_p and T_a/T_p, obtained by averaging the distributions shown in Figures 1(a) and (b) within each radial bin. The results reveal a clearer trend that has been described above: temperature ratio decreases as the radial distance increases, consistent with the previous studies (earlier Helios results in E. Marsch et al. 1982, and more recent PSP results in J. Peng et al. 2024). However, the anisotropy shows a trend that is opposite to the trend shown by the temperature, which is also consistent with the recent Wind observations (D. Stansby et al. 2019). A statistical comparison between both quantities yields a correlation coefficient of approximately −0.71, suggesting a clear anticorrelation between A_a/A_p and T_a/T_p. These results likely suggest that alpha particles experience a distinct thermodynamic evolution compared to protons: preferential perpendicular heating and stronger anisotropy close to the Sun are gradually offset, possibly by the expansion and the instability-driven relaxation as the solar wind propagates outward (L. Matteini et al. 2007; J. Huang et al. 2020).

To further investigate how the kinetic trends above depend on the solar wind stream structure, we partitioned the dataset

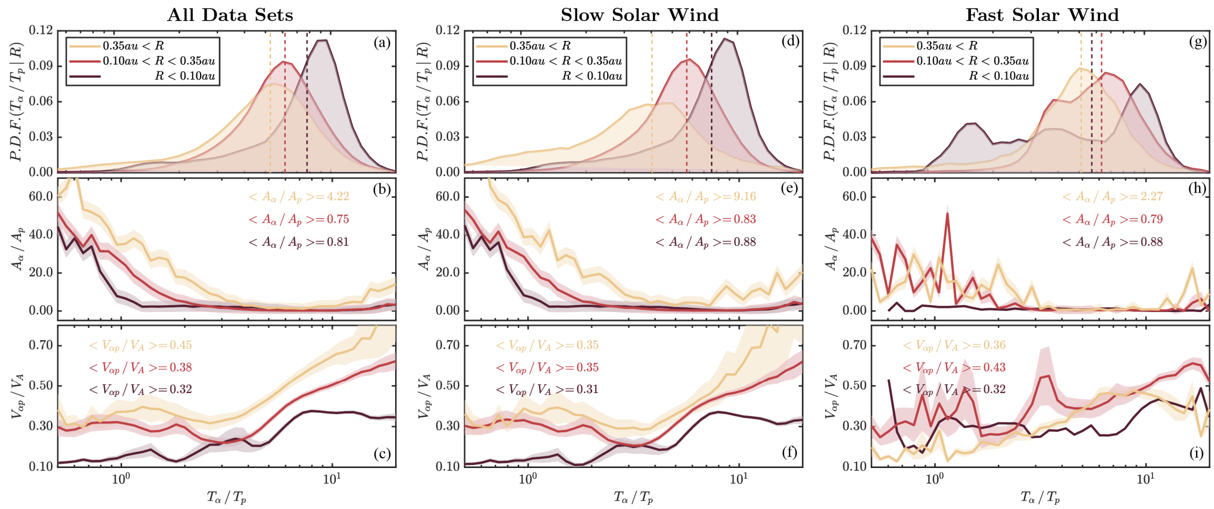

Figure 2. Relations of A_α/A_p and $V_{\alpha p}/V_A$ with T_α/T_p. The three columns are the results from (a)–(c) all datasets, (d)–(f) slow solar wind, and (g)–(i) fast solar wind. (a), (d), and (g) show pdfs of T_α/T_p in three regions: radial distance $R > 0.35$ au (yellow curve), 0.1 au $< R <$ 0.35 au (red curve), and $R < 0.1$ au (maroon curve). The vertical dashed lines mark the averaged value of the corresponding region. Distributions of A_α/A_p (b), (e), (h) and $V_{\alpha p}/V_A$ (c), (f), (i) with T_α/T_p are shown. The shaded regions are the error bars of standard deviation.

into slow ($\leqslant$400 km s^{-1}) and fast ($\geqslant$600 km s^{-1}) solar wind regimes, presented in Figures 1(d)–(i), respectively. The evolutionary trends in the slow wind closely mirror those of the aggregate dataset (Figures 1(a)–(c)), indicating that our overall statistical results are predominantly determined by slow wind intervals. In the fast regime, the anisotropy ratio A_a/A_p is systematically lower than in the slow wind, which aligns well with recent findings (V. K. Jagarlamudi et al. 2025). Furthermore, the anticorrelation between A_a/A_p and T_a/T_p is markedly stronger in the slow wind compared to the fast wind. This anticorrelation suggests that the energy partitioning mechanisms are regime dependent. In the highly structured, dynamically older slow wind, localized wave–particle interactions appear to efficiently couple perpendicular heating with parallel temperature relaxation. Conversely, the steady Alfvénic turbulence and distinct radial expansion profile characteristic of the fast wind may partially decouple these kinetic signatures.

To explore how the ion-heating behavior depends on R, we divide our dataset into three radial regions: $R < 0.1$ au (the near-Sun region), 0.1 au $< R <$ 0.35 au (the mid–inner heliosphere region), and $R > 0.35$ au (the more distant outer region), which are marked by the vertical dashed lines in Figure 1(c). These thresholds are chosen based on the radial positions where recent studies have revealed transitions in magnetic field fluctuations and spectral characteristics (D. Telloni et al. 2021; T. Alberti et al. 2022; J. Šafránková et al. 2023). Furthermore, each of the regions is characterized by a distinct $<T_\alpha/T_p>$ value, representing different turbulence or thermal environments in the expanding solar wind. This allows us to examine whether the alpha-particle heating process exhibits systematic differences across them.

Figure 2 presents results comparing the behaviors of the three regions above as functions of T_α/T_p. The pdfs of T_α/T_p in each region are shown in Figure 2(a). The near-Sun region (maroon curve) is characterized by higher T_α/T_p, and the peak shifts toward larger values compared to the mid and outer regions. The width of the distribution narrows moving from the outer region (yellow curve) to the near-Sun region, indicating reduced scatter in T_α/T_p close to the Sun. This narrowing suggests that the near-Sun environment would impose more constrained conditions on the heating processes of alpha particles.

Figure 2(b) shows the relationship between the averaged A_α/A_p and the T_α/T_p in each region. Contrary to an increasing trend, it suggests that the stronger A_α/A_p corresponds to lower T_α/T_p. As T_α/T_p increases (for example, beyond 4), the averaged A_α/A_p gradually approaches unity or even lower than 1, which also can be informed by the overall averaged A_α/A_p values noted in Figure 2(b). This result may suggest that when alpha particles become much hotter than protons, their anisotropy relative to protons diminishes. Furthermore, Figure 2(c) displays the results associated with normalized $V_{\alpha p}$. All three curves show the tendency that larger T_α/T_p are correlated with higher $V_{\alpha p}$ (Q. Y. Xiong et al. 2024a). It suggests that the relative velocity between alpha particles and protons increases concurrently with enhanced relative alpha heating, an effect that persists across varying radial distances. However, at smaller heliocentric distances, the differential velocity is observed to be smaller. This smaller velocity difference likely reflects the evolutionary state of the solar wind rather than relative heating, where preferential acceleration mechanisms have not yet fully developed the large differential drifts observed further outward.

Similar to our approach in Figure 1, we applied the same velocity partitioning to investigate the relationship between relative heating and anisotropy, presenting the slow and fast regimes in Figures 2(d)–(i), respectively. The isolated slow solar wind data are very similar to the aggregate dataset (Figures 2(a)–(c)), exhibiting an even more pronounced decrease in relative anisotropy at high T_α/T_p. Conversely, this trend is absent in the fast solar wind regime. This confirms that the overall behavior shown above is dominated by the slow solar wind bias. The prominence of this trend in the slow wind implies that its specific kinetic environment, characterized by highly structured and evolved turbulence, efficiently couples extreme preferential heating with a rapid reduction in relative temperature anisotropy. In contrast, our results indicate that this strong coupling does not manifest in the fast solar wind, where these kinetic signatures remain largely independent.

Observations show that alpha-particle heating exhibits a clear dependence on the local thermal state of the solar wind. Specifically, the narrowing of the T_α/T_p distribution toward smaller radial distances further indicates that the heating of alpha particles becomes increasingly regulated in regions where T_α/T_p is already enhanced. Moreover, the positive correlation between T_α/T_p and the differential velocity $V_{\alpha p}$ suggests that the relative drift between alpha particles and protons plays a significant role in contributing the interspecies energy exchange. These features could be interpreted to show that the observed regulation of alpha-particle heating may arise from kinetic processes such as temperature-anisotropy or drift-driven instabilities, including Alfvén/ion-cyclotron (A/IC) and fast magnetoionic/whistler (FM/W) modes (S. P. Gary et al. 2000a; D. Verscharen et al. 2013). To further verify the mechanisms responsible for the observed correlations above and to examine how differential flow and turbulence jointly influence alpha–proton energy partition, we attempt to employ fully kinetic PIC simulations in the following section.

3. Simulations

We use 2.5D (two-dimensional spatial positions and three-component vectors of fields and velocities) collisionless simulations with a fully kinetic PIC code (Q. Y. Xiong et al. 2023, 2024b, 2025) to study the particle heating in turbulence. The simulation domain is located on the *X*–*Z* plane, and *Y* is the out-of-plane direction along which variables have no changes. The simulation domain is $L = L_x = L_z = 64d_p$, where d_p is the proton inertial length and equals 32 cell lengths (Δ). Each cell contains 1600 positively charged particles, with the corresponding number of electrons enforcing quasi-neutrality. Among them, the alpha species occupy 5% of the total positive particles. Besides, the electrons are given an artificial mass ($m_e/m_p = 0.04$) for a reduced computational cost, while the alpha particles are assigned the realistic mass ratio $m_\alpha/m_p = 4$ and charge $q_\alpha/q_p = 2$. The initial electron beta value is $\beta_{e0} = 0.5$, and the temperature ratio between protons and electrons is $T_{p0}/T_{e0} = 1$.

The simulation is initialized with a uniform background magnetic field B_0 in the *Y* direction. The magnetic perturbations are constructed as a superposition of Fourier modes (V. Roytershteyn et al. 2019) expressed as $\delta\boldsymbol{B} = \psi_0 B_0 \boldsymbol{\sigma}_k \cos(\boldsymbol{k}\cdot\boldsymbol{x} + \phi_k)$, where ψ_0 is the perturbation amplitude, $\boldsymbol{\sigma}_k$ defines the polarization vector, and $\boldsymbol{k}$ and ϕ_k denote the wavevector and random phase of each mode. Here, the wavevector $\boldsymbol{k} = \{2\pi k_x/L_x,\ 2\pi k_z/L_z\}$, where $k_x = -6 \cdots 6$ and $k_z = 0 \cdots 6$. A corresponding ion's flow velocity perturbation $\delta\boldsymbol{V} = \psi_0 v_A \boldsymbol{\sigma}_k \cos(\boldsymbol{k}\cdot\boldsymbol{x} + \phi_k)$ (where $v_A = B_0/\sqrt{4\pi n_p m_p}$ is the initial proton Alfvén speed and n_p is the proton density) is simultaneously imposed on both proton and alpha species initially, which ensures the correlation between magnetic and velocity fluctuations. The amplitude of the perturbations above is chosen such that $|\delta B|^2/B_0^2 = |\delta V|^2/v_A^2 = 1$, corresponding to a strongly Alfvénic fluctuation regime that characterizes near-Sun solar wind turbulence.

To investigate the influence of the alpha–proton temperature ratio on kinetic evolution and differential heating, four simulation runs are performed with initial temperature ratios $T_{\alpha 0}/T_{p0} = 1$, 2, 4, and 8. These values are chosen to represent distinct thermal conditions corresponding to low, moderate, high, and extremely high temperature ratio, respectively. The selected range is also motivated by solar wind observations, which commonly show that the distribution of T_α/T_p exhibits a pronounced peak near 1 and a secondary enhancement around values of 4 (J. C. Kasper et al. 2008; P. Tracy et al. 2015). The selected temperature ratios above approximately span the full range of values inferred from the observations shown in Figure 1. Therefore, this comprehensive parameter set enables a direct, quantitative comparison between our simulations and observations, revealing how varying initial thermal states govern the turbulent heating of distinct ion species in the near-Sun environment.

Figure 3(a) shows the time evolution of normalized thermal energy changes for both protons and alpha particles. Across all four runs, the proton results exhibit broadly similar behavior, where they are rapidly heated during the early phase ($t\Omega_{cp} < 75$, where Ω_{cp} is proton cyclotron frequency). Then, the heating rate gradually decreases, producing a relatively smooth monotonic increase in thermal energy throughout later simulation times. The minor difference in the proton results in the four runs is expected, since alpha particles constitute a small number of the total ions and therefore have limited dynamical influence on the proton population. The alpha-particle heating, however, shows an apparent dependence on $T_{\alpha 0}/T_{p0}$. As $T_{\alpha 0}/T_{p0}$ increases, the growth of alpha-particle thermal energy is noticeably slower, which indicates that the heating efficiency of alpha particles is restrained.

Figure 3(b) shows the evolution of alpha–proton anisotropy ratio increment, together with the alpha–proton differential drift normalized to the local Alfvén speed. For the anisotropy ratio, all curves exhibit a brief initial adjustment followed by a persistent rise, indicating a development of stronger alpha-particle anisotropy relative to protons as the turbulence evolves. However, the growth rate and the amplitude of this enhancement depend sensitively on $T_{\alpha 0}/T_{p0}$, where the run with larger $T_{\alpha 0}/T_{p0}$ develops a lower increment in A_α/A_p. As for the differential drift, both the rise rate and peak value of $V_{\alpha p}$ are nearly identical across runs during the early phase. After this stage, however, the curves begin to diverge. Runs with lower $T_{\alpha 0}/T_{p0}$ sustain higher $V_{\alpha p}$ for a longer period, whereas those with smaller ones show an earlier saturation and subsequent decay.

To analyze the ion properties under fully developed turbulence, we focus on a late-time interval spanning $t\Omega_{cp} = 225 \sim 275$ (highlighted by the blue blocks in Figures 3(a) and (b)), during which the system has evolved beyond the initial transient phase and reached a state of fully developed turbulence. Using all data within this window, we compute spatially averaged temperature ratios and anisotropy ratios as functions of $V_{\alpha p}/V_A$. The resulting distributions are shown in Figures 3(c) and (d).

Figure 3(c) presents the relationship between the normalized differential drift and the enhancement of the alpha–proton temperature ratio. For all four runs, the stronger drift is associated with greater relative heating of alpha particles compared to protons. This feature is consistent with previous results (D. Perrone et al. 2013; Q. Y. Xiong et al. 2024a). Meanwhile, this trend holds consistently over the entire drift range, suggesting that $V_{\alpha p}$ serves as a key indicator of the extent to which alpha particles are preferentially energized by the turbulent fields. However, the magnitude of this enhancement varies with $T_{\alpha 0}/T_{p0}$, where runs with larger $T_{\alpha 0}/T_{p0}$ exhibit significantly lower in T_α/T_p, implying that a hotter initial alpha-particle population gains less additional heating.

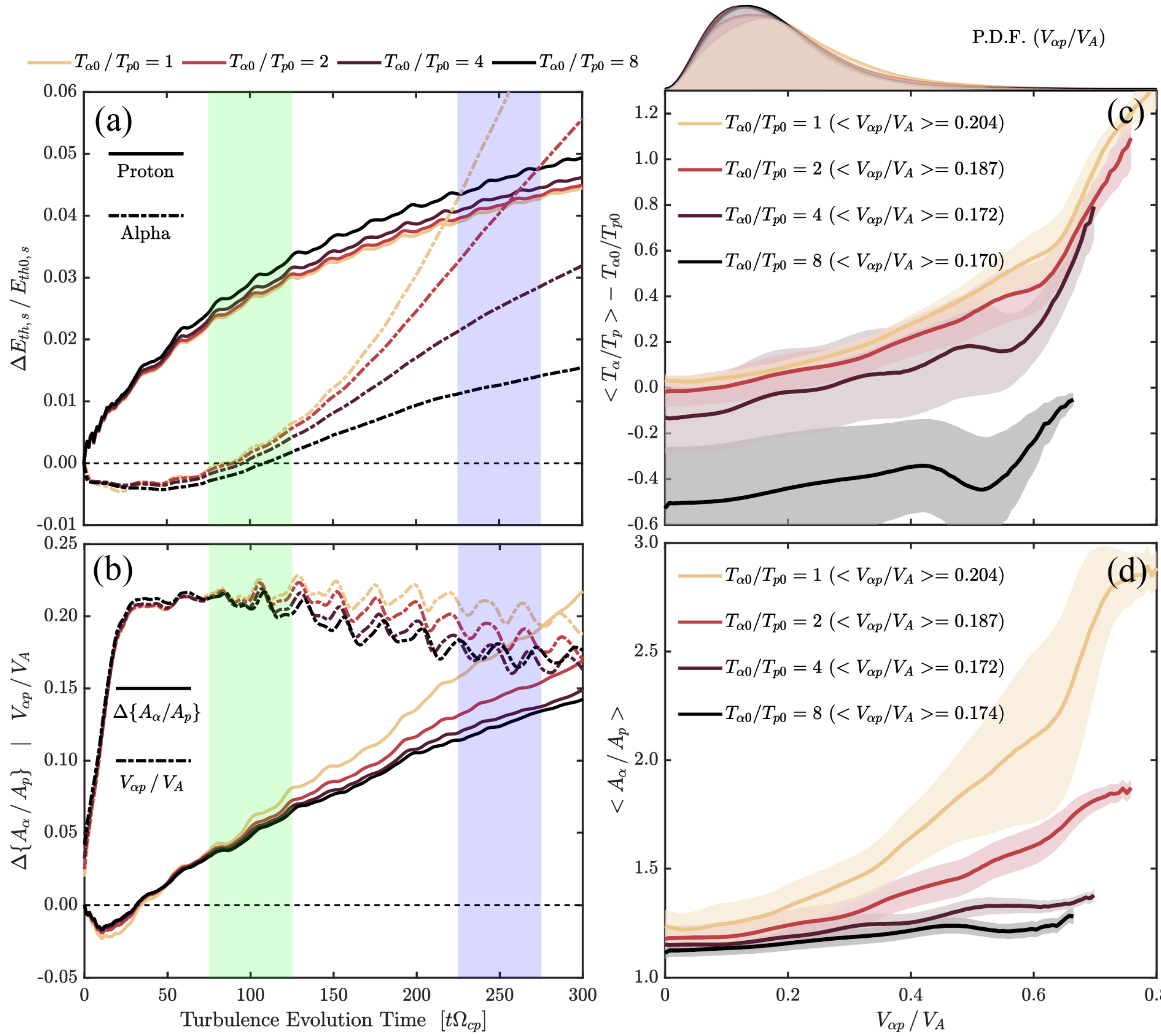

Figure 3. (a) Proton (solid curve) and alpha (dashed curve) normalized thermal energy change during the turbulence evolution. (b) A_α/A_p increment (solid curve) and $V_{\alpha p}/V_A$ (dashed curve) during the turbulent evolution. The time windows of green ($75 \sim 125\ t\Omega_{cp}$) and blue ($225 \sim 275\ t\Omega_{cp}$) shallow squares represent the early and later turbulence evolution phases, respectively. Different line colors represent different runs with corresponding initial temperature ratio, which is indicated above (a). Variations of temperature ratio increment (c) and temperature anisotropy A_α/A_p (d) with normalized alpha–proton differential drift $V_{\alpha p}/V_A$ in the later phase are shown. The shaded regions are the error bars of standard deviation.

Figure 3(d) reveals a similar correlation between the drift and the relative anisotropy. As the alpha–proton differential motion increases, the A_α/A_p also increases. One potential explanation for this relative enhancement is a species-dependent heating process. For example, turbulent fluctuations or instabilities driven by the differential flow (such as A/IC modes) could preferentially heat alpha particles in the perpendicular direction while interacting differently with protons. Therefore, this behavior implies that the processes responsible for generating the differential flow might also contribute to the distinct directional energization observed between the two species. Nevertheless, the degree of anisotropy enhancement is again strongly modulated by $T_{\alpha0}/T_{p0}$, where runs with higher initial alpha-particle temperature display more depressed anisotropy growth, indicating that elevated alpha-particle thermal speeds diminish their ability to acquire additional anisotropic heating from turbulence.

Our simulation results exhibit a positive correlation between T_α/T_p, A_α/A_p, and $V_{\alpha p}/V_A$. This trend contrasts with previous solar wind observations (S. Bourouaine et al. 2011a, 2011b; V. K. Jagarlamudi et al. 2025), which demonstrate an inverse relationship where enhanced alpha heating corresponds to depleted differential flow. We attribute this difference to the fundamental distinction between the instantaneous kinetic processes captured in our local simulations and the quasi-relaxed macroscopic state measured by spacecraft. In the solar wind, substantial differential flows provide a source of free energy that excites local plasma instabilities; the subsequent wave–particle scattering preferentially heats the alpha particles while simultaneously decelerating them and exhausting the drift speed (S. P. Gary et al. 2000b; J. C. Kasper et al. 2008; L. Matteini et al. 2012). Since this process acts on a short timescale compared to the timescale associated with the formation of these structures, observations frequently sample bulk plasma where this energy transfer has already occurred. Conversely, our collisionless simulations capture the dynamically active turbulence. Within this environment, localized patches of enhanced $V_{\alpha p}/V_A$ represent active sites of wave–particle interactions, driving immediate, localized alpha heating before the system fully relaxes.

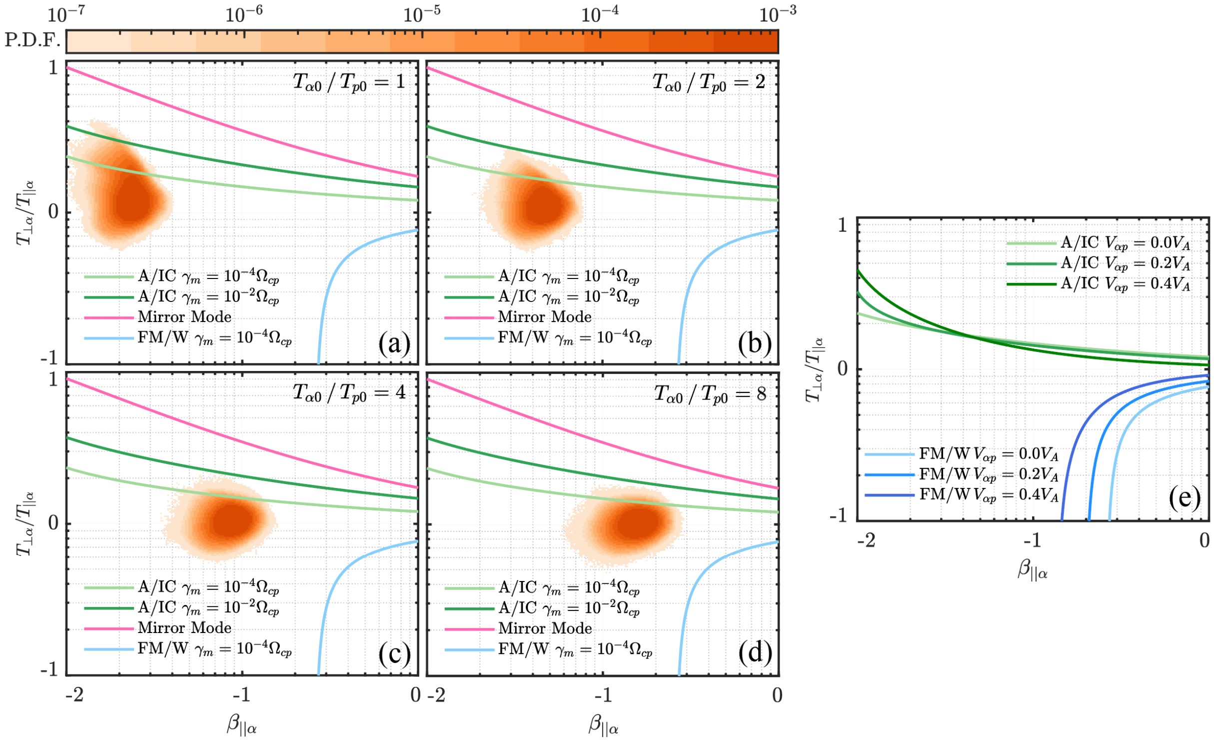

Figure 4. (a)–(d) Colored patches are the distributions of alpha particles of different runs. The curves with different colors mark the thresholds of different instability, which are indicated at the corner of each subfigure. (e) Thresholds of A/IC and FM/W using different initial alpha–proton differential drift.

The simulations have demonstrated that the heating of alpha particles is strongly influenced by their initial thermal state. As the $T_{\alpha 0}/T_{p0}$ increases, alpha-particle heating efficiency is progressively reduced, leading to weaker anisotropy development and a more subdued differential drift. These trends suggest that the alpha-particle population's ability to interact with turbulent fluctuations diminishes with increasing initial thermal velocity, likely due to the reduced resonance between the turbulent structures and the ion distributions. To better understand the underlying processes, we now turn to the analysis of instabilities, which are known to play a crucial role in shaping ion dynamics in turbulent plasmas.

Next, we examine the alpha-particle temperature-anisotropy distributions during the early phase $t\Omega_{cp} = 75 \sim 125$ (highlighted by the green blocks in Figures 3(a) and (b)), when the simulations start diverging in their evolutions. Using the data within this interval, we construct the two-dimensional pdfs in the $(\beta_{||\alpha}, A_\alpha)$ plane, shown in Figure 4. Superposed are linear instability thresholds computed with NHDS (D. Verscharen & B. D. G. Chandran 2018) using parameters matches to each run. In all four cases, the alpha-particle pdfs remain below the mirror-mode boundary, indicating that mirror instability does not participate in regulating the distribution. By contrast, the pdfs, particularly in the $T_{\alpha 0}/T_{p0} = 1$ run, extend across the low-growth A/IC threshold ($\gamma_m = 10^{-4}\Omega_{cp}$) and approach portions of high-growth threshold ($\gamma_m = 10^{-2}\Omega_{cp}$) contour, whereas this overlap weakens as $T_{\alpha 0}/T_{p0}$ increases. This pattern suggests that weak A/IC activity may be preferentially triggered when alpha particles relatively begin to be colder, and thus could contribute to limiting their perpendicular anisotropy at an early stage of the turbulent evolution. Since this regime exhibits the strongest suppression of later alpha-particle heating and anisotropy growth, our findings indicate that A/IC regulation likely bridges the early phase distribution dynamics and the reduced alpha-particle energization seen in higher $T_{\alpha 0}/T_{p0}$ runs.

4. Conclusions and Discussion

Alpha particles, though comprising only a minor fraction of the solar wind, play a consequential role in mediating turbulent energy dissipation and regulating ion-scale heating. In this study, we identify a systematic dependence of alpha-particle heating and anisotropy development on the local thermodynamic state of the plasma, particularly the alpha–proton temperature ratio as well as the differential drift. Observational analysis from PSP reveals that alpha-particle heating and anisotropy are both suppressed in intervals with elevated T_α/T_p and are positively correlated with $V_{\alpha p}$, indicating a dynamic coevolution where alpha-particle energization, temperature ratios, and differential drift are tightly coupled. Complementary PIC simulations extend these findings by showing that higher $T_{\alpha 0}/T_{p0}$ leads to reduced alpha-particle heating, weaker anisotropy growth, and lower differential drift generation, and that these outcomes are linked to A/IC instability. Taken together, observations and simulations consistently indicate that alpha-particle heating in solar wind turbulence is not universal but regulated by species-dependent plasma conditions. These results highlight that the pathways of ion heating depend on the background temperature anisotropies between protons and alpha particles.

The observed decrease in T_α/T_p with increasing heliocentric distance in Figure 1 might not be exclusively attributed to a radial decline in preferential heating efficiency. As the solar wind expands, its thermodynamic evolution is also strongly governed by Coulomb collisional relaxation. Although the inner heliosphere is broadly weakly collisional, the cumulative effect of Coulomb collisions over macroscopic distances continuously acts to thermalize the ion species, driving their temperatures toward equilibrium ($T_\alpha/T_p \sim 1$). Consequently, the radial trends observed in the PSP data represent a fundamental physical competition: while local kinetic wave–particle interactions actively drive preferential alpha heating, the accumulative effect of collisions progressively erases these induced temperature differences (J. C. Kasper et al. 2008, 2017; B. A. Maruca et al. 2013; P. Mostafavi et al. 2024). Therefore, cumulative collisionality significantly contributes to the macroscopic reduction of the alpha-to-proton temperature ratio and must be accounted for alongside collisionless mechanisms.

Increasing the relative initial alpha-particle temperature produces two robust kinetic effects that suppress subsequent alpha-particle energization. First, a hotter alpha-particle population has a larger thermal speed and gyroradius, which weakens its resonant and stochastic coupling to ion-scale turbulent fluctuations. This reduced interaction efficiency is a well-known consequence of gyro-averaging and broadened resonance widths (e.g., P. A. Isenberg & B. J. Vasquez 2007; B. D. G. Chandran et al. 2010). A broader thermal distribution dictates that fewer particles occupy the specific resonant velocities, thereby reducing the total energy available for exchange via resonant wave–particle interactions. Second, for a population initialized with higher thermal energy, a given absolute energy gain corresponds to a smaller fractional increment. Therefore, both the relative heating and the growth of temperature anisotropy evolve more slowly. These combined effects explain why, in our simulations, higher $T_{\alpha 0}/T_{p0}$ leads to significantly weaker perpendicular heating, suppressed anisotropy growth, and a reduced sustained $V_{\alpha p}$ relative to the thermal speed. In contrast, runs with lower $T_{\alpha 0}/T_{p0}$ maintain stronger resonant coupling to turbulent structures and therefore develop larger fractional heating, anisotropy, and drift.

For alpha particles, the growth of anisotropy and differential drift is often regulated by proximity to the A/IC and mirror-mode instability thresholds. Linear kinetic theory (S. P. Gary et al. 1993, 2006; P. Hellinger et al. 2006; D. Verscharen et al. 2013, 2019) shows that the A/IC marginal-stability condition can be approximated by

$$\frac{T_{\alpha,\perp}}{T_{\alpha,\parallel}} - 1 \gtrsim \frac{S}{\beta_{\alpha,\parallel}^{a}} + b\frac{V_{\alpha p}}{v_{\alpha,\parallel}},$$

where $v_{\alpha,\parallel} \propto \sqrt{T_{\alpha,\parallel}/m_\alpha}$ is the alpha-particle thermal speed, and S, a, and b are varying fitting constants. The first term on the right-hand side captures the beta dependence and the second accounts for differential drift. When the initial alpha-particle temperature is increased, the corresponding rise in $\beta_{\alpha,\parallel}$ formally lowers the A/IC marginal-stability threshold, which would in principle make the plasma more susceptible to cyclotron-resonant growth of A/IC waves for a given anisotropy. However, in this regime the turbulence generates only weak perpendicular heating and produces smaller values of both $T_{\alpha,\perp}/T_{\alpha,\parallel}$ and $V_{\alpha p}/v_{\alpha,\parallel}$. These reductions in anisotropy and normalized drift dominate over the beta-driven lowering of the threshold, shifting the alpha-particle population farther from marginal A/IC conditions rather than closer. Thus, in the high $T_{\alpha 0}/T_{p0}$ cases, the suppressed energization limits all drivers of cyclotron-resonant growth of A/IC waves, and the plasma remains well within the stable region despite the nominal effect of higher $\beta_{\alpha,\parallel}$.

Conversely, when the initial alpha-particle temperature is small, the cyclotron resonance condition $\omega - k_\parallel V_{\alpha p} = \Omega_\alpha$ is satisfied at higher $k_\parallel$. At these higher $k_\parallel$, the turbulence retains substantial power, which enhances alpha-wave coupling and enables more efficient perpendicular heating. Therefore, the system remains A/IC stable and alpha particles receive stronger perpendicular heating. In addition, the smaller initial $v_{\alpha,\parallel}$ makes the drift-normalized ratio $V_{\alpha p}/v_{\alpha,\parallel}$ larger, strengthening the drift contribution in the A/IC threshold condition. Hence, the distribution moves closer to the A/IC marginal-stability boundary rather than farther from it. This proximity enhances the probability of A/IC-like regulation during the early phase. As a result, alpha particles in the low $T_{\alpha 0}/T_{p0}$ case remain both more strongly heated and more anisotropic.

Besides, the mirror-mode threshold (A. Hasegawa 1969; D. J. Southwood & M. G. Kivelson 1993) for alpha species $T_{\alpha,\perp}/T_{\alpha,\parallel} - 1 \gtrsim 1/\beta_{\alpha,\perp}$ depends primarily on pressure anisotropy, so the alpha-particle population in our simulations never approaches mirror-mode marginal stability despite developing moderate anisotropy. It is also consistent with observational studies showing that alpha-driven mirror modes are rare compared with A/IC modes (S. D. Bale et al. 2009; B. A. Maruca et al. 2012; B. L. Alterman et al. 2018). Therefore, the combined effect of increased thermal speed, reduced drift, and weakened resonant cyclotron interaction explains why a larger $T_{\alpha 0}/T_{p0}$ results in less efficient perpendicular heating. Consequently, this weaker heating prevents the alpha particles from developing sufficient anisotropy to be driven into the A/IC unstable regime. Conversely, a smaller $T_{\alpha 0}$ allows for stronger kinetic coupling, leading to rapid perpendicular energization that quickly pushes the alpha particles across the instability threshold.

Acknowledgments

This work was supported by the National Natural Science Foundation of China (42574215, 42430203), China Postdoctoral Program for Innovation Talents (BX20250162), and China Postdoctoral Science Foundation (2025M780368). D.V. is supported by STFC Consolidated Grant ST/W001004/1. The PIC simulations in this work were performed on the supercomputing system in the Supercomputing Center of Wuhan University.

ORCID iDs

Q. Y. Xiong https://orcid.org/0000-0003-1840-3281
S. Y. Huang https://orcid.org/0000-0002-3595-2525
G. Li https://orcid.org/0000-0003-4695-8866
J. S. He https://orcid.org/0000-0001-8179-417X
N. Bian https://orcid.org/0000-0003-0142-8669
D. Verscharen https://orcid.org/0000-0002-0497-1096
T. N. Parashar https://orcid.org/0000-0003-0602-8381
J. Zhang https://orcid.org/0000-0001-5111-2609
H. H. Wu https://orcid.org/0000-0003-0424-9228
K. Jiang https://orcid.org/0000-0001-7889-0507
H. W. Zhan https://orcid.org/0009-0002-4006-6162

References

Alberti, T., Benella, S., Consolini, G., et al. 2022, ApJL, 940, L13
Alexandrova, O., Saur, J., Lacombe, C., et al. 2009, PhRvL, 103, 165003
Alterman, B. L., Kasper, J. C., Stevens, M. L., & Koval, A. 2018, ApJ, 864, 112

Balbus, S. A., & Hawley, J. F. 1998, RvMP, 70, 1
Bale, S. D., Goetz, K., Harvey, P. R., et al. 2016, SSRv, 204, 49
Bale, S. D., Kasper, J. C., Howes, G. G., et al. 2009, PhRvL, 103, 211101
Biskamp, D. 2003, PPCF, 45, 1827
Bourouaine, S., Marsch, E., & Neubauer, F. M. 2011a, A&A, 536, A39
Bourouaine, S., Marsch, E., & Neubauer, F. M. 2011b, ApJL, 728, L3
Bowen, T. A., Bale, S. D., Bandyopadhyay, R., et al. 2021, GeoRL, 48, e2020GL090783
Bowen, T. A., Bale, S. D., Bonnell, J. W., et al. 2020, ApJ, 899, 74
Bruno, R., & Carbone, V. 2013, LRSP, 10, 2
Chandran, B. D. G., & Perez, J. C. 2019, JPlPh, 85, 4
Chandran, B. D. G., Pongkitiwanichakul, P., Isenberg, P. A., et al. 2010, ApJ, 722, 710
Chen, C. H. K., Klein, K. G., & Howes, G. G. 2019, NatCo, 10, 740
Frisch, U. 1995, Turbulence: The Legacy of A. N. Kolmogorov (Cambridge Univ. Press)
Fox, N. J., Velli, M. C., Bale, S. D., et al. 2016, SSRv, 204, 7
Gary, S. P., Fuselier, S. A., & Anderson, B. J. 1993, JGRA, 98, 1481
Gary, S. P., Lin, Y., & Dan, W. 2006, JGRA, 111, A06105
Gary, S. P., Yin, L., Winske, D., & Reisenfeld, D. B. 2000a, GeoRL, 27, 1355
Gary, S. P., Yin, L., Winske, D., & Reisenfeld, D. B. 2000b, JGRA, 105, 20989
Gary, S. P., Yin, L., Winske, D., et al. 2003, JGRA, 108, 1068
Greco, A., Artemyev, A., & Zimbardo, G. 2015, GeoRL, 42, 8280
Hadid, L. Z., Sahraoui, F., Kiyani, K. H., et al. 2015, ApJL, 813, L29
Halekas, J. S., Whittlesey, P., Larson, et al. 2020, ApJS, 246, 22
Hasegawa, A. 1969, PhFl, 12, 2642
He, J., Tu, C., Marsch, E., & Yao, S. 2012, ApJL, 745, L8
Hellinger, P., Matteini, L., Štverák, Š., et al. 2011, JGRA, 116, A09105
Hellinger, P., Travnicek, P., Kasper, J. C., & Lazarus, A. J. 2006, GeoRL, 33, L09101
Horbury, T. S., Forman, M., & Oughton, S. 2008, PhRvL, 101, 175005
Huang, J., Kasper, J. C., Vech, D., et al. 2020, ApJS, 246, 70
Huang, S. Y., Hadid, L. Z., Sahraoui, F., Yuan, Z. G., & Deng, X. H. 2017, ApJL, 836, L10
Huang, S. Y., Sahraoui, F., Andrés, N., et al. 2021, ApJL, 909, L7
Huang, S. Y., Xu, S. B., Zhang, J., et al. 2022, ApJL, 929, L6
Huang, S. Y., Zhang, J., Xiong, Q. Y., et al. 2023, ApJ, 958, 189
Isenberg, P. A., & Vasquez, B. J. 2007, ApJ, 668, 546
Jagarlamudi, V. K., Mostafavi, P., Palacios, J. C., et al. 2025, ApJL, 995, L68
Kasper, J. C., Abiad, R., Austin, G., et al. 2016, SSRv, 204, 131
Kasper, J. C., Klein, K. G., Lichko, E., et al. 2021, PhRvL, 127, 255101
Kasper, J. C., Klein, K. G., Weber, T., et al. 2017, ApJ, 849, 126
Kasper, J. C., Lazarus, A. J., & Gary, S. P. 2008, PhRvL, 101, 261103
Kasper, J. C., Stevens, M. L., Lazarus, A. J., et al. 2007, ApJL, 660, 901
Kiyani, K. H., Osman, K. T., & Chapman, S. C. 2015, RSPTA, 373, 20140155
Li, G., Miao, B., Hu, Q., & Qin, G. 2011, PhRvL, 106, 125001
Livi, R., Larson, D. E., Kasper, J. C., et al. 2022, ApJ, 938, 138
Maruca, B. A., Bale, S. D., Valvo-Sorriso, L., Kasper, J. C., & Stevens, M. L. 2013, PhRvL, 111, 241101
Maruca, B. A., Kasper, J. C., & Gary, S. P. 2012, ApJ, 748, 137
Marsch, E., Rosenbauer, H., Schwenn, R., et al. 1982, JGRA, 87, 35
Matteini, L., Hellinger, P., Travnicek, P., & Velli, M. 2012, SSRv, 172, 373
Matteini, L., Horbury, T. S., Pantellini, F., et al. 2015, ApJ, 802, 11
Matteini, L., Landi, S., Hellinger, P., et al. 2007, GeoRL, 34, L20105
Matthaeus, W. H., & Velli, M. 2011, SSRv, 160, 145
Matthaeus, W. H., Zank, G. P., Smith, C. W., & Oughton, S. 1999, PhRvL, 82, 3444
McComas, D. J., Barraclough, B. L., Funsten, H. O., et al. 2000, JGRA, 105, 10419
Mostafavi, P., Allen, R. C., Jagarlamudi, V. K., et al. 2024, A&A, 682, A152
Mostafavi, P., Allen, R. C., McManus, M. D., et al. 2022, ApJL, 926, L38
Mostafavi, P., Jagarlamudi, V. K., Raouafi, N. E., et al. 2025, ApJL, 991, L35
Müller, D., Cyr, O. C., Zouganelis, I., et al. 2020, A&A, 642, A1
Navarro, R. E., Muñoz, V., Valdivia, J. A., & Moya, P. S. 2020, ApJL, 898, L9
Neugebauer, M. 1981, FCPh, 7, 131
Ofman, L., Boardsen, S. A., Jian, L. K., et al. 2022, ApJ, 926, 185
Ofman, L., Vinas, A. F., & Roberts, D. A. 2017, JGRA, 122, 5839
Peng, J., He, J., Duan, D., & Verscharen, D. 2024, ApJ, 977, 27
Perrone, D., Valentini, F., Servidio, S., et al. 2013, ApJ, 762, 99
Perrone, D., Settino, A., Perri, S., et al. 2024, ApJ, 973, 171
Roytershteyn, V., Boldyrev, S., Delzanno, G. L., et al. 2019, ApJ, 870, 103
Šafránková, J., Němeček, Z., Němec, F., et al. 2023, ApJL, 946, L44
Sahraoui, F., Goldstein, M. L., Robert, P., & Khotyaintsev, Y. V. 2009, PhRvL, 102, 231102
Sahraoui, F., Huang, S. Y., Belmont, G., et al. 2013, ApJ, 777, 15
Schekochihin, A. A., Cowley, S. C., Dorland, W., et al. 2009, ApJS, 182, 310
Southwood, D. J., & Kivelson, M. G. 1993, JGRA, 98, 9181
Stansby, D., Perrone, D., Matteini, L., Horbury, T. S., & Salem, C. S. 2019, A&A, 623, L2
Telloni, D., Sorriso-Valvo, L., Woodham, L. D., et al. 2021, ApJL, 912, L21
Tracy, P., Kasper, J. C., Zurbuchen, H., et al. 2015, ApJ, 812, 170
Tu, C.-Y., & Marsch, E. 1995, MHD Structures, Waves and Turbulence in the Solar Wind: Observations and Theories (Springer)
Verscharen, D., Bourouaine, S., & Chandran, D. G. 2013, ApJ, 773, 163
Verscharen, D., & Chandran, B. D. G. 2018, RNAAS, 2, 13
Verscharen, D., Klein, K. G., & Maruca, B. A. 2019, LRSP, 16, 5
Woodham, L. D., Horbury, T. S., Matteini, L., et al. 2021, A&A, 650, L1
Xiong, Q. Y., Huang, S. Y., Yuan, Z. G., et al. 2023, ApJS, 263, 3
Xiong, Q. Y., Huang, S. Y., Yuan, Z. G., et al. 2024b, CoPhC, 295, 108994
Xiong, Q. Y., Huang, S. Y., Yuan, Z. G., et al. 2025, AIPA, 15, 025201
Xiong, Q. Y., Parashar, T. N., Huang, S. Y., et al. 2024a, ApJ, 968, 93
Yogesh, Ofman, L., Klein, K. G., et al. 2026, ApJ, 999, 225
Zhang, J., Huang, S. Y., He, J. S., et al. 2022, ApJL, 924, L21
Zhang, M. F., Kunz, M. W., Squire, J., & Klein, K. G. 2025, ApJ, 979, 121